INSTITUTE OF PHYSICS PUBLISHING SEMICONDUCTOR SCIENCE AND TECHNOLOGY

Semicond. Sci. Technol. **20** (2005) S228–S236 doi:10.1088/0268-1242/20/7/013

Resonant-phonon-assisted THz quantum-cascade lasers with metal–metal waveguides

Qing Hu[1], Benjamin S Williams[1], Sushil Kumar[1], Hans Callebaut[1], Stephen Kohen[1] and John L Reno[2]

[1] Department of Electrical Engineering and Computer Science and Research Laboratory of Electronics, Massachusetts Institute of Technology, Cambridge, MA 02139, USA
[2] Sandia National Laboratories, Department 1123, MS 0601, Albuquerque, NM 87185-0601, USA

Received 21 January 2005
Published 8 June 2005
Online at stacks.iop.org/SST/20/S228

Abstract

We report our development of terahertz (THz) quantum-cascade lasers (QCLs) based on two novel features. First, the depopulation of the lower radiative level is achieved through resonant longitudinal optical (LO-)phonon scattering. This depopulation mechanism is robust at high temperatures and high injection levels. In contrast to infrared QCLs that also use LO-phonon scattering for depopulation, in our THz lasers the selectivity of the depopulation scattering is achieved through a combination of resonant tunnelling and LO-phonon scattering, hence the term *resonant phonon*. This resonant-phonon scheme allows a highly selective depopulation of the lower radiative level with a sub-picosecond lifetime, while maintaining a relatively long upper level lifetime (>5 ps) that is due to upper-to-ground-state scattering. The second feature of our lasers is that mode confinement is achieved by using a novel double-sided metal–metal waveguide, which yields an essentially unity mode confinement factor and therefore a low total cavity loss at THz frequencies. Based on these two unique features, we have achieved some record performance, including, but not limited to, the highest pulsed operating temperature of 137 K, the highest continuous-wave operating temperature of 97 K, and the longest wavelength of 141 μm (corresponding to 2.1 THz) without the assistance of a magnetic field.

(Some figures in this article are in colour only in the electronic version)

1. Introduction

Terahertz (1–10 THz, $\hbar\omega = 4$–40 meV or $\lambda = 30$–300 μm) frequencies are among the most underdeveloped electromagnetic spectra, even though their potential applications are promising in detection of chemical and biological agents, imaging for medical and security applications, astrophysics, plasma diagnostics, end-point detection in dry etching processes, remote atmospheric sensing and monitoring, non-invasive inspection of semiconductor wafers, high-bandwidth free-space communications and ultrahigh-speed signal processing. This underdevelopment is primarily due to the lack of coherent solid-state THz sources that can provide high radiation intensities (greater than 1 mW) and continuous-wave (CW) operations. This is because the THz frequency falls between two other frequency ranges in which conventional semiconductor devices have been well developed. One is the microwave and millimetre-wave frequency range, and the other is the near-infrared and optical frequency range. Semiconductor electronic devices that utilize freely moving electrons (such as transistors, Gunn oscillators, Schottky-diode frequency multipliers and photomixers) are limited by the transit time and parasitic *RC* time constants. Consequently, the power level of these classical devices decreases as $1/f^4$, or even faster, as the

frequency f increases above 1 THz. In contrast to electronic devices that use freely moving electrons to generate radiation, photonic or quantum-electronic devices (such as laser diodes) generate radiation by oscillating bound charge carriers (which give rise to an oscillating displacement current). Consequently, they are not limited by the transient time and/or the *RC* time constants. However, for conventional bipolar laser diodes, they are limited to frequencies that correspond to the semiconductor energy gap, which is higher than 10 THz even for narrow-gap lead-salt materials. Thus, the frequency range below 10 THz is inaccessible for conventional semiconductor diode lasers.

Semiconductor quantum wells are man-made quantum-mechanical systems in which the energy levels can be designed and engineered to any value. Consequently, unipolar lasers based on intersubband transitions (electrons that make lasing transitions between subband levels within the conduction band or holes within the valence band) were proposed for long-wavelength sources as early as the 1970s [1]. However, because of the great challenge in epitaxial material growth and the unfavourable fast nonradiative relaxation rate, it took more than two decades to realize this proposal experimentally. Electrically pumped unipolar intersubband-transition lasers (also called quantum-cascade lasers (QCLs)) at $\sim$4 μm wavelength were first developed at Bell Laboratories in 1994 [2]. Since then, impressive improvements in performance have been made in terms of power levels, operating temperatures and frequency characteristics at mid-infrared frequencies.

In contrast to the remarkable development of mid-infrared QCLs, the development of THz QCLs below the *Reststrahlen* band ($\sim$8–9 THz in GaAs) turned out to be much more difficult than initially expected [3], because of two unique challenges at THz frequencies. First, the energy level separations that correspond to THz frequencies are quite narrow ($\sim$10 meV). Thus, the selective depopulation mechanism based on energy-sensitive longitudinal optical (LO-)phonon scattering, which has been successfully implemented in mid-infrared QCLs, is not applicable. Second, low-loss optical mode confinement, which is essential for any laser oscillation, is difficult to achieve at THz frequencies. Conventional dielectric-waveguide confinement cannot be used because the evanescent field penetration, which is proportional to the wavelength and is of the order of several tens of micrometres, is much greater compared to the active gain medium thickness of several micrometres.

In October 2001, almost eight years after the initial development of QCLs, the first QCL operating below the *Reststrahlen* band, at 4.4 THz, was developed [4]. This laser was based on a chirped-superlattice structure that had been successfully developed at mid-infrared frequencies [5]. Mode confinement in this THz QCL was achieved using a double-surface plasmon waveguide grown on a semi-insulating (SI) GaAs substrate. Shortly after this breakthrough, a very similar laser structure was developed at 4.6 THz [6]. Following that work, the same group developed THz QCLs based on a bound-to-continuum intersubband transition, which have yielded higher operating temperatures and output power levels than those based on chirped- superlattice structures [7].

Our group has pursued a different approach to achieve lasing at THz frequencies. We have investigated possibilities of using fast LO-phonon scattering to depopulate the lower radiative level [8, 9], and using double-sided metal–metal waveguides for THz mode confinement [10]. After an extensive investigation, these efforts finally bore fruit. In November 2002, a 3.4 THz QCL was developed in which the depopulation of the lower radiative level was achieved through resonant LO-phonon scattering [11]. The performance of this laser device was promising, especially in its maximum operating temperature. A laser device fabricated from the first wafer operated in the pulse mode up to 87 K, producing more than 4 mW of peak power at liquid-nitrogen temperature [12]. When fabricated with the double-sided metal–metal waveguides, QCLs based on similar quantum-well structures have demonstrated the highest pulsed operating temperature of 137 K, the highest CW operating temperature of 97 K, and the longest wavelength of 141 μm without the assistance of magnetic fields. In a parallel effort, we have analysed the transport properties of our THz QCL structures using Monte Carlo (MC) simulations [13, 14]. In this analysis, we have identified leakage current channels that should be minimized in order to reduce the lasing threshold current densities and to improve the laser performance. We summarize key results of these investigations in the following sessions.

2. THz gain medium based on resonant LO-phonon scattering for depopulation

The unipolar intersubband lasers are known to yield a high value of gain, because of a large joint density of states as a result of the two subbands tracking each other in the $\vec{k}$-space; thus electrons emit photons at the same energy regardless of their initial momentum. Consequently, the peak gain is related to the inverted population density Δn_{3D} in a simple linear fashion:

$$g_{\text{peak}} = \Delta n_{3D} \frac{e^2 \omega}{\pi \hbar \varepsilon_r^{1/2} \varepsilon_0 c_0} \frac{z_{ij}^2}{\Delta f} = \Delta n_{3D} \frac{e^2}{2\pi \varepsilon_r^{1/2} \varepsilon_0 c_0 m^*} \frac{f_{ij}}{\Delta f}$$
$$\approx 67(\Delta n_{3D}/10^{15}\ \text{cm}^{-3}) \frac{f_{ij}}{\Delta f/\text{THz}}\ \text{cm}^{-1}. \quad (1)$$

In equation (1), Δn_{3D} is the three-dimensional inverted population density in the active region, $z_{ij} = \langle i|z|j\rangle$ is the dipole moment and $f_{ij} = \left(2m^*\omega z_{ij}^2\right)/\hbar$ is the dimensionless oscillator strength of the $i \rightarrow j$ transition. Δf is the FWHM linewidth of spontaneous emission in units of Hz (but in units of THz in the last numerical part of equation (1)). Clearly from equation (1), there are only three parameters that determine the peak material gain, Δn_{3D}, Δf and f_{ij}, whereas all other parameters are either fundamental constants or material parameters that are not subject to engineering and manipulation. In our structures, the measured spontaneous emission linewidth Δf is usually close to 1 THz ($\sim$4 meV). The main task of our design process has been to optimize the other two parameters, Δn_{3D} and f_{ij}.

From the relation $f_{ij} = \left(2m^*\omega z_{ij}^2\right)/\hbar$, to the leading degree, the oscillator strength is determined by the spatial overlap of the two subband wavefunctions that gives a good measure of the radiative dipole moment z_{ij}. Thus, in order to achieve a large value of f_{ij}, the radiative transition should be made spatially vertical. The population inversion Δn_{3D} ($=\Delta n_{2D}/$(thickness of the active region)) is mainly determined

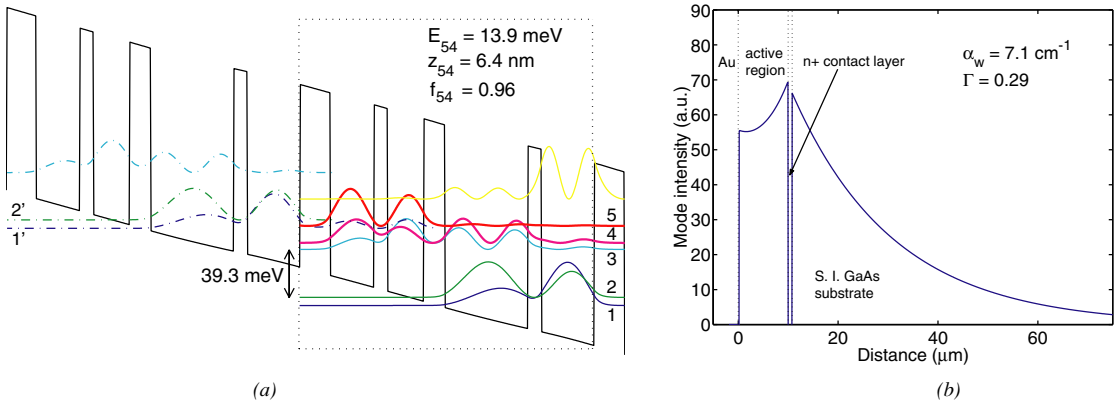

Figure 1. (*a*) Conduction band profile calculated using a self-consistent Schrödinger and Poisson solver at a bias of 64 mV/module, which corresponds to a field of 12.2 kV cm^{-1}. The four-well module is outlined. Beginning with the left-injection barrier, the layer thicknesses in Å are **54**/78/**24**/64/**38**/148/**24**/94, where bold fonts represent barrier thicknesses. The 148 Å well is doped at 1.9×10^{16} cm^{-3}, yielding a sheet density of 2.8×10^{10} cm^{-2}. (*b*) Optical mode profile of the plasmon waveguide.

by the lifetimes of the lower radiative state τ_l, the upper radiative state τ_u and the upper-to-lower state scattering time $\tau_{u\to l}$. A large Δn_{3D} requires a short τ_l, and long τ_u and $\tau_{u\to l}$. The nonradiative relaxation time $\tau_{u\to l}$, can be made long at the cost of reducing the oscillator strength f_{ij}. $\tau_{u\to l}$ is also determined by the electron temperature, density and the lasing frequency. Its optimization requires detailed analysis of individual structures. The focus of our investigation has been on reducing τ_l and enhancing τ_u. In order to reduce τ_l, the lower radiative level should be coupled strongly to the ground states, while in order to increase τ_u, the upper radiative state should be isolated as much as possible from the ground states.

Our first design addressed this consideration by making the optical transition diagonal (i.e. between states in adjacent wells), so as to reduce upper-state overlap with the collector state [8]. However, this resulted in a small oscillator strength, and a broad emission linewidth due to interface roughness. A second design featured a vertical radiative transition [9], which improved the radiative overlap and had a relatively narrow linewidth (∼2 meV ≈ 0.5 THz), but depopulation of the lower state was nonselective and slow, due to the thick barrier needed to reduce parasitic scattering from the upper state.

The key element in our current design is to use *resonant LO-phonon scattering* to selectively depopulate the lower radiative level while maintaining a long upper level lifetime. This resulted in a breakthrough success. Figure 1(*a*) shows the conduction band profile and subband wavefunctions under the design bias of 64 mV/module. Each module contains four quantum wells, shown inside the dashed box, and 175 such modules are connected in series to form the quantum-cascade laser. Under this bias, the electrons are injected from the injector level $1'$ to the upper lasing level 5 through resonant tunnelling. The radiative transition between levels 5 and 4 is spatially vertical, yielding a relatively large oscillator strength ($f_{54} \approx 0.96$). The depopulation is highly selective and fast, as only the lower level 4 is at resonance with a level 3 in the adjacent well, where fast LO-phonon scattering ($\tau_4 \approx \tau_3 \approx$ 0.5 ps) takes place to empty electrons in levels 3 and 4 to the injector doublet 1 and 2. Due to a relatively thick barrier, the scattering time of the upper level 5 to the ground states 2 and 1 is quite long ($\tau_{5\to 2,1} \approx 7$ ps), which is important to maintain a population inversion between levels 5 and 4. Electrons in level 1 are then injected to level 5 of the following module (not shown here), completing the cascade pumping scheme.

Mode confinement in this laser device was achieved using a double-surface plasmon waveguide formed between the top metallic contact and the bottom heavily doped GaAs layer, as in the case of other THz QCLs [4, 6]. The calculated mode profile and waveguide loss are shown in figure 1(*b*). The calculated waveguide loss of 7.1 cm^{-1} and mode confinement factor $\Gamma \approx 29\%$ are favourable compared to the calculated gain of our laser device. After the rear facet was high-reflection (HR) coated, lasing was obtained in this device and a typical emission spectrum above threshold is shown in figure 2(*a*). The emission frequency corresponds to a photon energy of 14.2 meV, close to the calculated value of 13.9 meV. Pulsed lasing operation is observed up to 87 K with a power level (measured using a calibrated thermopile detector, ScienTech Model 360203) of 13 mW at 5 K, and ∼4 mW even at liquid-nitrogen temperature of 78 K, as shown in figure 2(*b*) [12].

The maximum temperature of pulsed operation of this first THz QCL device is encouraging. However, compared to the chirped-superlattice and bound-to-continuum THz QCLs, the threshold current density in this laser is quite high (∼800 A cm^{-2}), which causes a significant heating at high duty cycle operations. The main reason of this high threshold current density is a leakage channel, which we have identified with the aid of Monte Carlo simulations [13]. It is clear from figure 1 that at certain voltage ranges below the designed bias, the injector level $1'$ is actually aligned with the level 3 that is primarily located in the widest well where fast LO-phonon scattering takes place. Because of this fast scattering, the current density at this bias is quite high, as can be seen from the shoulder structure in the *V–I* curve in figure 2(*b*) at ∼10 V and ∼600 A cm^{-2}. The device must be biased beyond this point to inject electrons into the upper level 5, and thus with a positive dynamic conductance (which is required for a stable dc bias), the lasing threshold current density will be at least as high as this value. Reduction of this leakage channel and

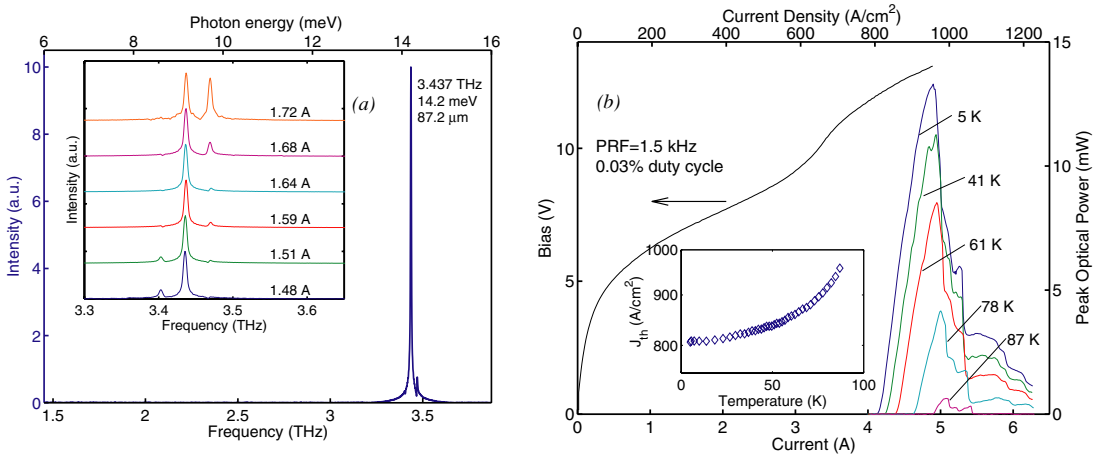

Figure 2. (*a*) Emission spectrum above threshold. The inset shows a set of emission spectra that are Stark-shifted to higher frequencies with higher bias. The linewidth is limited by the instrumental resolution of the FTIR (0.125 $cm^{-1} = 3.75$ GHz). (*b*) Pulsed power–current relations taken from a similar laser device at different heat sink temperatures.

therefore threshold current density has been a main objective of our current investigation. This leakage channel can be reduced by careful design of the injector and active region to reduce the coupling between levels $1'$ and 3, when these two levels are energetically aligned.

3. THz mode confinement using metal–metal waveguides

Because of the amphoteric nature of silicon dopants in GaAs materials, the maximum attainable electron density is approximately 5×10^{18} cm^{-3}. At this carrier concentration, the field penetration depth is of the order of 1 μm at THz frequencies, causing a significant cavity loss if the lower side of the mode confinement is provided by heavily doped GaAs layers [15, 16]. The first successful development of THz QCLs utilized a double-surface plasmon layer grown on a semi-insulating GaAs substrate for mode confinement [4, 6]. As illustrated in figure 1(*b*), the presence of the n^+ bottom contact layer enhances the mode intensity in the active region. Although the mode still extends substantially into the substrate, the overlap with heavily doped regions is small, so the free-carrier loss is minimized. This structure is easy to grow and fabricate, and it provides adequate mode confinement for most of the THz QCLs. However, the mode confinement factor Γ in this scheme is far below unity ($\Gamma \sim 0.2$–0.5 for reported lasers). At longer wavelengths ($\lambda > 100$ μm), Γ will become even smaller because of two factors. First, the geometric effect of a longer wavelength reduces the overlap. Second, the dielectric constant $\varepsilon(\omega)$ in the lightly doped active region is reduced by a factor $\left(1 - \omega_p^2/\omega^2\right)$ as the frequency ω approaches the plasma frequency $\omega_p = (ne^2/m^*\varepsilon)^{1/2}$. The reduction of $\varepsilon(\omega)$ in the active region compared to that of the SI substrate will further reduce the confinement factor.

Following our initial success in developing the 3.4 THz laser, we demonstrated the first terahertz QCL that uses a double-sided metal–metal waveguide for mode confinement [17]. This metal–semiconductor–metal structure is essentially the same as the microstrip transmission lines that are widely used for waveguiding at microwave and millimetre-wave frequencies, and the geometry is compatible with the TM polarization of intersubband transitions. Due to the shallow skin depth in the metal (several hundred Å), the waveguide can be made with very low losses and a confinement factor close to unity. In an earlier effort, we developed a process to fabricate such metal–metal waveguide structures using a combination of wafer bonding and selective etching [10]. Enhanced THz electroluminescence, but not lasing, was observed in such structures [18]. Mid-infrared QCLs have also been demonstrated using a metal waveguide fabricated via a solder-bonding method. However, at such high frequencies (>12 THz), the loss at the metal surface (scaled as $\omega^{1/2}$) becomes significant so that the metal waveguide QCLs actually performed slightly worse than those using the conventional mid-infrared single-sided surface plasmon waveguides [19]. A detailed analysis of comparative performance of the metal–metal waveguides and double-surface plasmon waveguides will be published elsewhere [20].

Our first THz laser with a metal–metal waveguide was fabricated using low temperature In–Au metallic wafer bonding followed by substrate removal. The schematic of the bonding and substrate removal process is illustrated in figure 3. Before bonding, the MBE-grown wafer was prepared by evaporating Ti/Au layers. An n^+ GaAs receptor substrate was coated with the metal sequence Pd/Ge/Pd/In. The purpose of the Pd/Ge/Pd multilayer was to improve the electrical contact to the receptor substrate [21]. Wafer pieces of about 1 cm^2 were cleaved, aligned and bonded on a hot plate at 250 °C for ∼10 min while pressure was applied to the stack. Bonding takes place above the melting point of In (157 °C) as the indium wets the surface to fill in any crevices, and then diffuses into the gold layer to reactively form a variety of In–Au alloys [22, 23]. By careful choice of the metallic layer composition, all of the elemental indium will be consumed, and the bonding layer formed by the In–Au alloys remains robust up to their melting points (∼450 °C).

Based on this metal–metal waveguide structure and using improved gain media that reduced the aforementioned parasitic current channel, and therefore the lasing threshold current

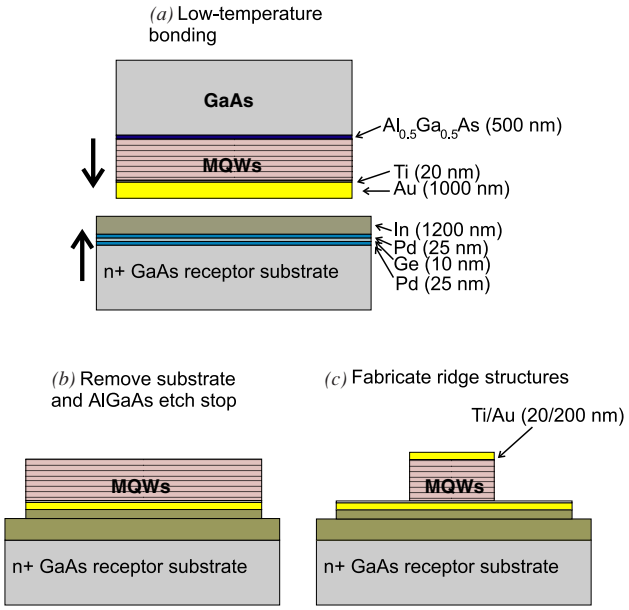

Figure 3. Schematic of the wafer bonding process for the double-side metal–metal waveguide.

densities, we have achieved several records in the performance of THz QCLs. These include the highest pulsed operating temperature of 137 K (figure 4(*a*)) [24], the first CW THz QCL operating above the important liquid-nitrogen temperature of 77 K (figure 4(*b*)) [25], and the longest wavelength QCL to date without the assistance of magnetic fields ($\lambda \approx 141$ μm, corresponding to 2.1 THz (figure 4(*c*)) [26].

Recently, following the developments at another MIT group that has developed copper-to-copper wafer bonding for vertical chip integration [27], we have fabricated metal–metal waveguides using the copper-to-copper thermocompression bonding technique. Compared to the In–Au alloy wafer bonding used earlier, copper has higher electrical and thermal conductivities than those of In–Au alloy. Both are desired in the reduction of the lasing threshold and a more robust CW operation at high temperatures. Figure 5(*a*) shows the SEM picture of a laser facet of a metal–metal waveguide fabricated using copper-to-copper wafer bonding. It shows that the laser bar was cleaved nicely along with the supporting substrate, and the bonded copper layers are of good quality. Figure 5(*b*) shows the results from a 25 μm wide and 1.04 mm long laser device fabricated using copper-to-copper bonding. The width of 25 μm is the narrowest among THz QCLs, and at this width only one lateral waveguide mode is supported by the structure. In fact, at the lasing wavelength of $\lambda \approx 107$ μm, the ratio of width/λ is the lowest of any laser structures. This is largely due to the fact that the metal–metal waveguide provides a strong mode confinement in the lateral direction, as well as in the vertical direction as shown in figure 5(*a*). With such a small width and length, the threshold current is only $\sim$80 mA at low temperatures, which results in $<$1 W power dissipation. As a result of this low power dissipation at the threshold and a good wafer bonding quality, the maximum CW operating temperature (97 K) of this device is only lower by 16 K from its maximum pulsed operating temperature (113 K). This result represents the state-of-the-art in terms of the highest CW operating temperature of THz QCLs.

4. Analysis of transport properties of the THz QCLs based on Monte Carlo simulations

Despite the similarity between mid-infrared and THz QCLs, there is a qualitative difference in their dynamics of electron transport. For mid-infrared QCLs, the radiative transition energy $\hbar\omega$ exceeds the LO-phonon energy $\hbar\omega_{\rm LO}$ ($\hbar\omega_{\rm LO} =$ 36 meV in GaAs) and electron transport is dominated by LO-phonon scattering, which is only weakly temperature dependent and density independent. As a result, the analysis of the mid-infrared QCLs is usually based on a conventional rate-equation approach, in which all the lifetimes are assumed to be constant. In the THz frequency range, however, where $\hbar\omega < \hbar\omega_{\rm LO}$, only the high-energy tail of a hot electron distribution is subject to the LO-phonon scattering, which results in a significantly enhanced temperature sensitivity for the electron transport and a far greater importance of electron–electron (e–e) scattering. If a rate-equation approach is used to analyse the transport properties of THz QCLs, then many of the lifetimes are no longer constant and they depend on the injection levels of the device under operation, thus making the rate equations highly nonlinear. The long delay in the development of THz QCLs is testimony to the difficulty of achieving population inversion involving these complicated transport mechanisms. It is thus important to be able to quantitatively model these transport processes for the design of suitable THz QCLs for operations at broader frequency ranges and higher temperatures.

Our transport analysis is based on MC simulations, which have been used to analyse and design mid-infrared and THz QCLs [28, 29]. Compared to the conventional rate-equation analysis, the MC method is especially useful for THz QCLs, as it does not rely on a specific assumption for carrier distributions and can easily handle temperature- and density-dependent scattering times. The MC simulation follows a conventional scheme for an ensemble ($\sim 10^4$) of particles, with a focus on e–e, electron–phonon (e–ph) and electron–impurity (e–imp) interactions involving the electrons in one module of the device under study. Only interactions with electrons in states belonging to the same or a neighbouring module are considered. An electron that scatters out of a module is re-injected with identical in-plane $\vec{k}$-vector into a subband equivalent to its destination subband, in accordance with the spatial periodicity of the QCLs [28].

Using this numerical simulation tool, we have analysed transport properties of many intersubband THz emitters, including our own devices and other published ones in the literature. Because of the availability of detailed experimental results, here we focus mainly on the 3.4 THz QCL structure shown in figure 1(*a*), with the key results summarized in figure 6. We used a 25 K lattice temperature throughout the simulation that accounts for a temperature rise during a 100 ns pulse operation with a heat sink temperature of 5 K.

In figure 6(*a*), a noticeable feature is that the calculated current density at the designed bias of 65 mV/module is significantly lower than the measured one if e–imp scattering is

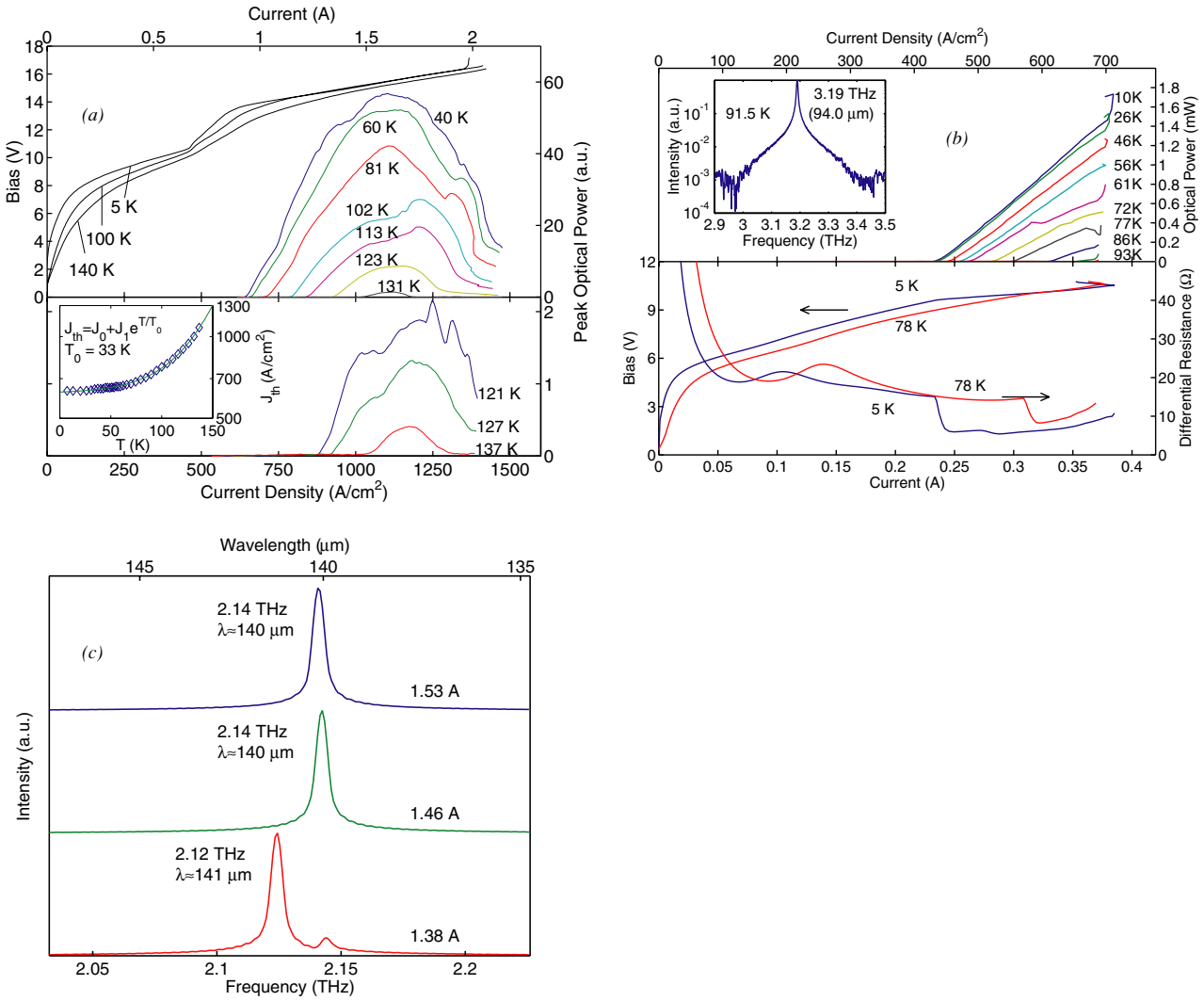

Figure 4. (*a*) Pulsed power–current and voltage–current relations measured up to ∼137 K heat sink temperature. (*b*) CW power–current and voltage–current relations measured up to ∼93 K heat sink temperature. (*c*) Lasing emission spectra at 2.1 THz.

not included (represented by circles). The agreement between the calculated and measured current densities becomes much better if the e–imp scattering is included. This scattering mechanism increases the current density and lowers the upper-state population in two ways. First, it directly scatters electrons down from an upper level. Second, the extra kinetic energy acquired by an electron scattered down from an upper level will heat up the electron gas via electron–electron scattering. As a result of this elevated electron temperature, thermally activated LO-phonon scattering from the upper level will be increased [14].

In figure 6(*a*), the first increase in current density occurs in a bias range of ∼35–45 mV/module where the injector level $n = 1'$ becomes aligned with $n = 3$, which is primarily located in the widest well where fast LO-phonon scattering takes place. The narrow anticrossing gap between these two levels (∼0.6 meV) indicates that the calculated peak current density of nearly 2000 A cm^{-2} at ∼45 mV/module (not shown) is a severe overestimation, as wavefunction localization due to dephasing in real devices reduces the coupling between $n = 1'$ and $n = 3$. Still, this parasitic channel carries a significant amount of current, as is evident from the experimentally observed current shoulder at ∼45 mV/module. This detailed transport analysis points out the direction to reduce the threshold current density—this parasitic channel must be reduced significantly. This can be achieved by decreasing the coupling between the injector ground state and the upper LO-phonon resonant state by adding more wells to the active or injector regions, or alternatively by increasing the thickness of the barriers between these two states.

At biases exceeding 50 mV/module, the $n = 2'$ and $n = 1'$ doublet injects carriers into the upper radiative level $n = 5$, yielding a gain as shown in figure 6(*d*). The injector ground state $n = 1'$ and $n = 5$ line up at the designed bias of 65 mV/module, reaching the maximum available gain of ∼70 cm^{-1}. In comparison, we achieved lasing from a 1.18 mm long Fabry–Perot ridge with one facet HR coated (facet loss $\alpha_m = \ln(1/R)/2L$), but no lasing with both facets uncoated ($\alpha_m = \ln(1/R)/L$). Hence the peak gain value is bounded by the total cavity losses of these two structures, shown as the two horizontal lines in figure 6(*d*). As shown in figure 6(*d*), the

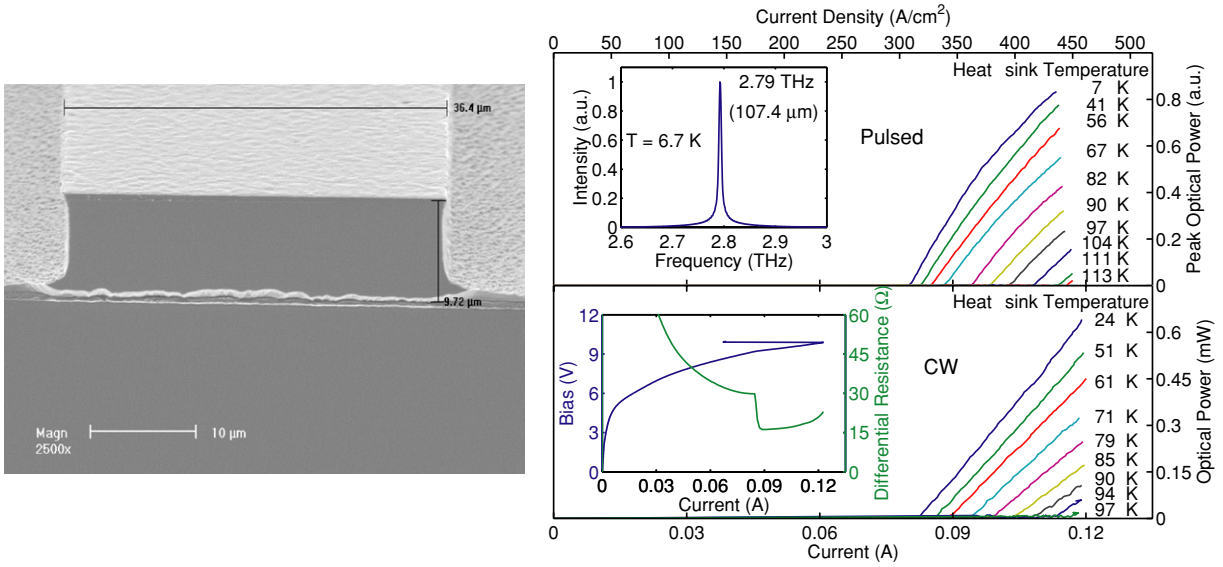

(a) *(b)*

Figure 5. (*a*) SEM picture of a laser facet from a device using copper-to-copper wafer bonding. (*b*) Light–current (*L–I*) relations of pulsed (upper panel) and CW (lower panel) operations from a 25 μm wide and 1.04 mm long laser device. The inset in the upper panel shows the lasing frequency at ∼2.79 THz. The inset in the lower panel shows the *V–I* and d*V*/d*I–I* relations of the laser device under CW operation.

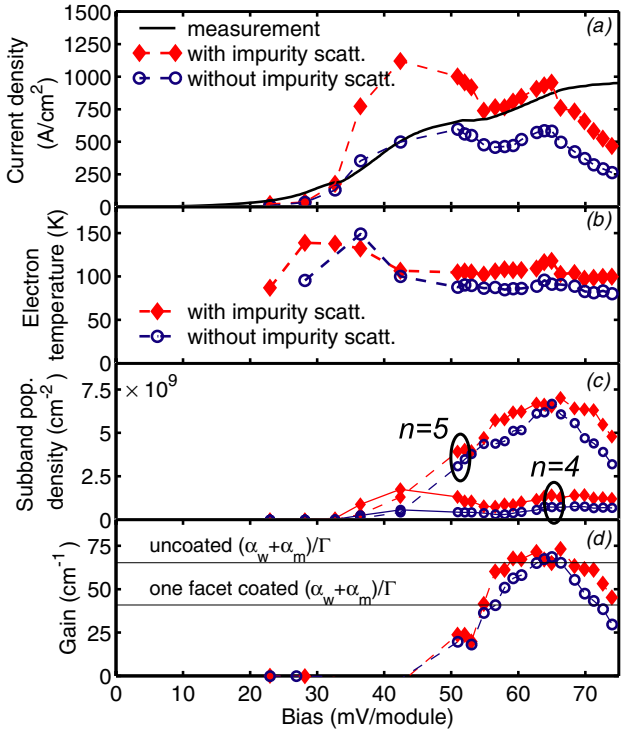

Figure 6. In (*a*)–(*d*), circles are the results calculated without including electron–impurity scattering and diamonds are the results with electron–impurity scattering. (*a*) Current density for a range of biases. The injection anticrossing occurs at 65 mV/module. The measured current is represented as a full line. A large parasitic current peak of ∼2000 A cm^{-2} at ∼45 mV/module was omitted from the simulation results. (*b*) Electron temperature T_e for the subbands involved in the radiative transition, $n = 4$ and $n = 5$. (*c*) The population density in $n = 4$ and $n = 5$. (*d*) Material gain for different biases. Also indicated are the calculated threshold gain values for a 1180 × 150 μm^2 ridge structure, with uncoated facets and with one facet HR coated.

calculated maximum gain slightly exceeds the upper bound of the range inferred from the measured results.

Despite the reasonably good agreement shown in figure 6, however, a challenging problem remains in our transport analysis of how to deal with wavefunction localization caused by dephasing scattering. In all the MC studies on transport properties in QCL structures, the entire multiple quantum-well structure is treated as a single quantum-mechanical system, for which Schrödinger's equation is solved to yield spatially extended subband states. In general, coherent interaction and time evolution is ignored, and transport is modelled as intersubband scattering among these spatially extended states, in a way similar to the Boltzmann transport equation. In this Boltzmann-like picture, potential barriers do not cause any bottlenecks in the transport process. For example, a thicker injection barrier only yields a smaller anticrossing gap, and thus will not affect the peak current density at resonance but will only make the resonance sharper. In this picture, both the injection to the upper radiative level and removal of electrons from the lower radiative level tend to be quite efficient at resonance. As a result, our transport analysis based on this Boltzmann-like model predicted appreciable levels of gain in most of the structures that we have experimentally investigated for THz lasing. In real devices, however, dephasing scattering (due to interface roughness, alloy and impurity scatterings) interrupts the coherent interactions between states and effectively localizes wavefunctions, making transport between weakly coupled states (characterized by a small anticrossing gap between these states) mostly an incoherent tunnelling process. This incoherent sequential tunnelling process is much less efficient than the injection and removal rates predicted by the Boltzmann-like model. Despite the optimistic predictions from the Boltzmann-like model, in our experimental investigations only quantum-well structures

similar to that shown in figure 1 have achieved lasing. A THz quantum-cascade laser based on an interlaced photon–phonon cascade was developed recently [30]. However, its maximum operating temperature (∼95 K) is notably lower than those of lasers based on resonant LO-phonon scattering. Although other factors may be at play (for example, different waveguides were used), one could speculate that the depopulation in the interlaced photon–phonon lasers is not as efficient as predicted by the Boltzmann-like model, as the electrons in the lower lasing state have to tunnel through several barriers before encountering LO-phonon scattering. A possible solution to deal with the problem of wavefunction localization is to start from a tight-binding model in a density-matrix formalism. In this model, the dephasing scattering damps the Rabi oscillation between two states across an energy barrier and therefore it comes in naturally in the reduction of the coupling/transport among spatially localized basis states [1]. It is a challenging task to incorporate this model in a Monte Carlo simulation tool, especially for complicated structures that include many quantum wells even in one module. Another possible approach is based on a non-equilibrium Green's function theory. Although not as intuitive as the MC approach, it takes all the dephasing processes into account and calculates important parameters such as the gain and current density [31]. Both tasks are presently under investigation.

Acknowledgments

We would like to thank S Goodnick for generously allowing us to adapt his Monte Carlo simulation code, and A Fan for helping us in fabricating metal–metal waveguides using the copper-to-copper wafer bonding technique. This work is supported by AFOSR, NASA and NSF. Sandia is a multiprogramme laboratory operated by the Sandia Corporation, a Lockheed Martin Company, for the United States Department of Energy's National Nuclear Security Administration under contract no DE-AC04-94AL85000.

References

[1] Kazarinov R F and Suris R A 1971 Possibility of the amplification of electromagnetic waves in a semiconductor superlattice *Sov. Phys.—Semicond.* **5** 707

[2] Faist J, Capasso F, Sivco D L, Sirtori C, Hutchinson A L and Cho A Y 1994 Quantum cascade laser *Science* **264** 477

[3] Helm M, England P, Colas E, DeRosa F and Allen S J Jr 1989 Intersubband emission from semiconductor superlattices excited by sequential resonant tunneling *Phys. Rev. Lett.* **63** 74

[4] Köhler R, Tredicucci A, Beltram F, Beere H E, Linfield E H, Davies A G, Ritchie D A, Iotti R C and Rossi F 2002 Terahertz semiconductor-heterostructure laser *Nature* **417** 156

[5] Tredicucci A *et al* 1998 High performance interminiband quantum cascade lasers with graded superlattice *Appl. Phys. Lett.* **73** 2101

[6] Rochat M, Ajili L, Willenberg H, Faist J, Beere H, Davies G, Linfield E and Ritchie D 2002 Low-threshold terahertz quantum-cascade lasers *Appl. Phys. Lett.* **81** 1381

[7] Scalari G, Ajili L, Faist J, Beere H, Davies G, Linfield E and Ritchie D 2003 Far infrared ($\lambda \approx 86$ μm) quantum-cascade lasers based on bound-to-continuum transition with operation temperature up to 90 K *Appl. Phys. Lett.* **82** 3165

[8] Xu B, Hu Q and Melloch M R 1997 Electrically pumped tunable terahertz emitter based on intersubband transition *Appl. Phys. Lett.* **71** 440

[9] Williams B S, Xu B, Hu Q and Melloch M R 1999 Narrow-linewidth terahertz intersubband emission from three-level systems *Appl. Phys. Lett.* **75** 2927

[10] Xu B 1998 Development of intersubband terahertz lasers using multiple quantum well structures *PhD Thesis* MIT

[11] Williams B S, Callebaut H, Kumar S, Hu Q and Reno J L 2003 3.4-THz quantum cascade laser based on LO-phonon scattering for depopulation *Appl. Phys. Lett.* **82** 1015
Williams B S, Callebaut H, Kumar S, Hu Q and Reno J L 2003 3.4-THz quantum cascade laser based on LO-phonon scattering for depopulation *Virtual J. Nanoscale Sci. Technol.* **7** (24 February)

[12] Williams B S, Kumar S, Callebaut H, Hu Q and Reno J L 2003 3.4-THz quantum cascade lasers operating above liquid-nitrogen temperatures *Electron. Lett.* **39** 915

[13] Callebaut H, Kumar S, Williams B S and Reno J L 2003 Analysis of transport properties of THz quantum cascade lasers *Appl. Phys. Lett.* **83** 207

[14] Callebaut H, Kumar S, Williams B S, Hu Q and Reno J L 2004 Importance of electron–impurity scattering for electron transport in terahertz quantum-cascade laser *Appl. Phys. Lett.* **84** 645

[15] Hu Q and Feng S 1991 Feasibility of far-infrared lasers using multiple semiconductor quantum wells *Appl. Phys. Lett.* **59** 2923

[16] Rochat M, Beck M, Faist J and Oesterle U 2001 Measurement of far-infrared waveguide loss using a multisection single-pass technique *Appl. Phys. Lett.* **78** 1967

[17] Williams B S, Kumar S, Callebaut H, Hu Q and Reno J L 2003 3.0-THz ($\lambda = 100$ μm) quantum-cascade laser using metal waveguide for mode confinement *Appl. Phys. Lett.* **83** 2124

[18] Williams B S 2003 Terahertz quantum cascade lasers *PhD Thesis* MIT

[19] Unterrainer K, Colombelli R, Gmachl C, Capasso F, Hwang H Y, Sergent A M, Sivco D L and Cho A Y 2002 Quantum cascade lasers with double metal–semiconductor waveguide resonators *Appl. Phys. Lett.* **80** 3060

[20] Kohen S, Williams B S and Hu Q 2005 Electromagnetic modeling of terahertz quantum cascade laser waveguides and resonators *J. Appl. Phys.* **97** 053106

[21] Wang L C, Wang X Z, Lau S S, Sands T, Chen W K and Kuech T F 1990 Stable and shallow PdIn ohmic contacts to *n*-GaAs *Appl. Phys. Lett.* **56** 2129

[22] Lee C C, Wang C Y and Matijasevic G 1993 Au-In bonding below the eutectic temperature *IEEE Trans. Compon. Hybrids Manuf. Technol.* **16** 311

[23] Wang T B, Shen Z Z, Ye R Q, Xie X M, Stubhan F and Freytag J 2000 Die bonding with Au/In isothermal solidification technique *J. Electron. Mater.* **29** 443

[24] Williams B S, Kumar S, Callebaut H, Hu Q and Reno J L 2003 Terahertz quantum cascade lasers operating up to 137 K *Appl. Phys. Lett.* **83** 5142

[25] Kumar S, Williams B S, Kohen S, Hu Q and Reno J L 2004 Continuous-wave operation of terahertz quantum-cascade lasers above liquid-nitrogen temperature *Appl. Phys. Lett.* **84** 2494

[26] Williams B S, Kumar S, Hu Q and Reno J L 2004 Resonant-phonon terahertz quantum-cascade laser operating at 2.1 THz ($\lambda \approx 141$ μm) *Electron. Lett.* **40** 431

[27] Chen K N, Fan A, Tan C S, Reif R and Wen C Y 2002 Microstructure evolution and abnormal grain growth during copper wafer bonding *Appl. Phys. Lett.* **81** 3774

[28] Iotti R C and Rossi F 2001 Carrier thermalization versus phonon-assisted relaxation in quantum-cascade lasers: a Monte Carlo approach *Appl. Phys. Lett.* **78** 2902

[29] Köhler R, Iotti R C, Tredicucci A and Rossi F 2001 Design and simulation of terahertz quantum cascade lasers *Appl. Phys. Lett.* **79** 3920

[30] Köhler R, Tredicucci A, Mauro C, Beltram F, Beere H E, Linfield E H, Davies A G and Ritchie D A 2004 Terahertz quantum-cascade lasers based on an interlaced photon–phonon cascade *Appl. Phys. Lett.* **84** 1266

[31] Lee S-C and Wacker A 2003 Theoretical analysis of spectral gain in a terahertz quantum-cascade laser: prospects for gain at 1 THz *Appl. Phys. Lett.* **83** 2506